Advanced Intelligent Discovery

WILEY VCH

ADVANCED INTELLIGENT DISCOVERY Open Access

RESEARCH ARTICLE OPEN ACCESS

Machine-Learning-Based, Feature-Rich Prediction of Alumina Microstructure from Hardness

Xiao Geng[1] | Jianan Tang[2,3] | Ningxuan Wen[2,3] | Jason Shaw[2,4] | Siddhartha Sarkar[1] | Lionel Vargas-Gonzalez[5] | Nicholas Ku[5] | Jianhua Tong[1] | Rajendra K. Bordia[1] | Dongsheng Li[6] | Fei Peng[1,3]

[1]Department of Materials Science and Engineering, Clemson University, Clemson, South Carolina, USA | [2]Department of Electrical and Computer Engineering, Clemson University, Clemson, South Carolina, USA | [3]Center for Optical Materials Science and Engineering Technologies (COMSET), Clemson University, Anderson, South Carolina, USA | [4]Christ Church Episcopal School, Greenville, South Carolina, USA | [5]Ceramics and Transparent Materials Branch, DEVCOM Army Research Laboratory, Aberdeen, Maryland, USA | [6]Advanced Manufacturing LLC, East Hartford, Connecticut, USA

Correspondence: Fei Peng (fpeng@clemson.edu)

Received: 14 November 2024 | **Revised:** 24 March 2025 | **Accepted:** 7 April 2025

Funding: US Army, Grant/Award Number: W911NF-23-2-0058; US Department of Energy, National Energy Technology Lab, Grant/Award Number: DE-FE0032231; US Department of Energy, Office of Energy Efficiency & Renewable Energy, Grant/Award Number: DE-EE0011323; US National Institute of Health, Grant/Award Number: P20GM121342; US National Science Foundation, Grant/Award Number: 2119833

Keywords: additive manufacturing | inverse prediction | machine learning | microstructure image prediction

ABSTRACT

Predicting materials' microstructure from the desired properties is critical for exploring new materials. Herein, a novel regression-based prediction of scanning electron microscopy (SEM) images for the target hardness using generative adversarial networks (GANs) is demonstrated. This article aims at generating realistic SEM micrographs, which contain rich features (e.g., grain and neck shapes, tortuosity, spatial configurations of grain/pores). Together, these features affect material properties but are difficult to predict. A high-performance GAN, named 'Microstructure-GAN' (or M-GAN), with residual blocks to significantly improve the details of synthesized micrographs is established . This algorithm was trained with experimentally obtained SEM micrographs of laser-sintered alumina. After training, the high-fidelity, feature-rich micrographs can be predicted for an arbitrary target hardness. Microstructure details such as small pores and grain boundaries can be observed even at the nanometer scale (∼50 nm) in the predicted 1000× micrographs. A pretrained convolutional neural network (CNN) was used to evaluate the accuracy of the predicted micrographs with rich features for specific hardness. The relative bias of the CNN-evaluated value of the generated micrographs was within 2.1%–2.7% from the values for experimental micrographs. This approach can potentially be applied to other microscopy data, such as atomic force, optical, and transmission electron microscopy.

1 | Introduction

Predicting the required microstructure for specific properties provides an important tool for designing novel materials. Many materials' properties are strongly influenced by microstructure [1–3]. For instance, the hardness and yield strength of alloy increases with reducing grain size, following the Hall–Petch relation [4]. The conductivity of ceramic electrolytes is strongly affected by grain size distribution [5, 6]. The porosity has dominant effects on the catalytical performance and conductivity of ceramic electrodes [7, 8] and the hardness and elastic properties of ceramics [9, 10]. Thus, predicting the microstructure for the needed properties can significantly accelerate material discovery.

In material science, machine-learning (ML) techniques have been developed as a powerful tool in microstructure predictions [11–14]. The typical ML-based microstructure prediction is

focused on descriptors prediction [11, 12]. A descriptor distribution usually represents a certain aspect of manually extracted microstructural features [15, 16]. After training, ML models can directly generate end-to-end solutions. For example, the microstructure features of cold-roll metal, such as volume ratios of different steel phases, were used as descriptors and were inversely predicted from the strain–stress curve. These descriptors usually represent certain microstructural features. However, it is difficult to construct or generate actual material microstructure inversely from descriptor distributions.

Microstructural images, usually experimentally obtained from microscopy (e.g., scanning electron microscope (SEM)), are good representations of actual microstructure. They contain visualizable details, such as grain/pore shapes and sizes, tortuosity, local surface topography, and shape information that cannot be easily extracted. All these rich features can affect materials' properties, which are hard to completely describe by descriptors. Therefore, generating micrographs from the target properties is crucial in high-fidelity microstructure inverse prediction.

Recently, generative adversarial networks (GANs) [17] have shown significant potential for generating realistic microstructural images [13–15, 18]. A typical GAN has two convolutional neural networks (CNN): generator and discriminator. The generator is trained to mimic actual image samples, while the discriminator is trained to distinguish the generated samples from real ones. The generator can produce high-fidelity images once this adversarial training process is completed.

Using GAN to predict microstructure or structure for the desired properties has been limited due to the lack of experimental SEM micrographs for training. In the available studies, physical models were used first to establish the training data of correlated microstructure and properties [19–21]. In one study, the Cahn–Hilliard microstructure was used to simulate the short-circuit current density (J_{sc}) and fill factor (FF) of a solar cell [19]. In another study, an invariance network (InvNet) was established to achieve inverse microstructure prediction of organic photovoltaic systems for target performance. InvNet was modified from WGAN (GAN using Wasserstein distance) and owned one more pretrained CNN, which outputs invariance constraint to the generator [20]. In another study, the training data for the microstructure was generated using a random boundary method. The homogenized elastic modules of the microstructures were calculated using the homogenization method. The inverse microstructure prediction for target performance was achieved using a conditional WGAN with gradient penalty [21].

In the aforementioned studies, the simulated microstructures are often oversimplified and do not represent the rich features of the actual microstructure obtained experimentally (e.g., SEM images). The properties of different microstructures are usually calculated from physical models or the finite-element method. Thus, this approach of using simulated data of microstructure and property for ML training cannot explore the relationship between property and microstructure without known governing laws.

In this study, ML-based prediction of feature-rich realistic microstructures for desired properties, trained from the experimental data, has been demonstrated. Based on the experimental dataset, we established an ML-guided method to inversely predict realistic SEM micrographs for targeted properties (i.e., hardness). The data of SEM micrographs of laser-sintered alumina and corresponding hardness were collected using our laser-based high-throughput sample array fabrication and characterization [22]. The ML algorithm was based on our previously published regression-based, conditional Wasserstein GAN with gradient penalty (RCWGAN-GP) [18, 23], which achieved good microstructure prediction for unknown processing parameters or sensing signals for laser-sintered ceramics. In this study, we modified our networks with residual blocks to improve the synthesis quality and named the new algorithm *M-GAN* ("M" refers to microstructure). As a result, the realistic microstructure micrographs, which have a similar quality to the experimental obtained SEM images, can be predicted for the target hardness. Compared to RCWGAN-GP and other classic GAN-based algorithms mentioned previously, the microstructure micrographs with larger image sizes (256×256 pixels) can be predicted with high fidelity in M-GAN. Smoother and clearer grain features were observed, and the noise in synthesized images was eliminated. Recognizable microstructure features can be nanometer scale ($\approx$50 nm) in 12.8×12.8 μm micrographs. The accuracy of predictions from M-GAN was evaluated by a pretrained CNN. The relative bias of all regenerated images was within 4.9%. The relative bias of prediction for target hardness was 2.1% for the high-hardness sample and 2.7% for the low-hardness one. They all indicate high accuracy and good robustness for the M-GAN prediction. Because the training of M-GAN was only based on experimental datasets, the inverse microstructure prediction can be easily achieved on other material systems and for other microstructure-sensitive properties. As a result, when applied to the unknown microstructure–properties relationship in advanced materials, the M-GAN can create new opportunities for inverse material design and advanced material exploration.

2 | Results and Discussion

2.1 | The GAN-Based ML Algorithms and Training Datasets

We compared the performances of three GAN-based ML algorithms of inverse microstructure prediction for target hardness. These algorithms all have a similar structure, shown in Figure 1. These three ML algorithms are (1) RCWGAN-GP, (2) RCWGAN-GP-W, and (3) M-GAN (or M-GAN). The RCWGAN-GP is reported in our previous study, which refers to 'regression-based conditional generative adversarial network (CGAN) with Wasserstein loss function and gradient penalty' [18]. In this article, we doubled the network width of both generator and discriminator of RCWGAN-GP and named this network 'RCWGAN-GP-W' ('W' stands for wide). For the third ML algorithm, we augmented the network structure of the RCWGAN-GP algorithm with residual blocks. A residual block utilizes skip connections to increase the depth of a neural network without diminishing the backpropagating gradients. Literature shows that residual blocks can improve the generated image quality [24, 25]. We adjusted our new algorithm, especially for microstructure prediction. Thus, it is named 'Microstructure-GAN'

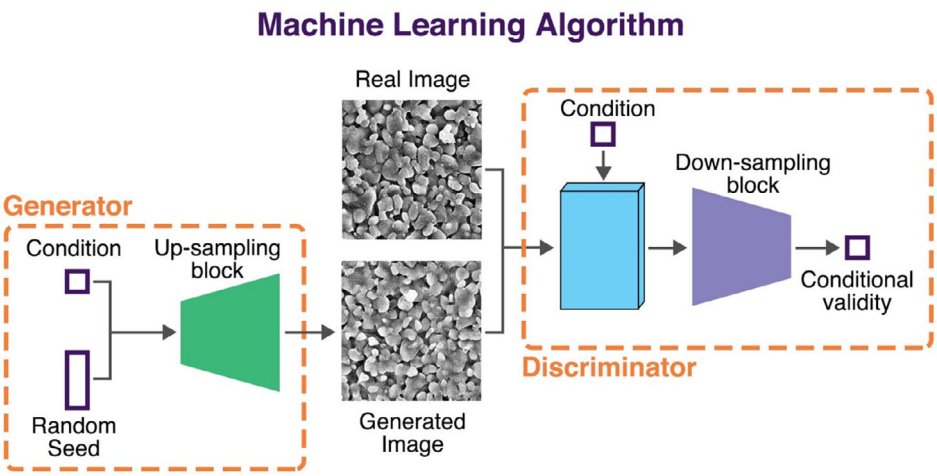

FIGURE 1 | Illustration of GAN-based ML algorithms of microstructure prediction for target properties. In these algorithms, the property (i.e., hardness) is the condition.

or 'M-GAN.' The detailed architectures of these three algorithms and the training process are given in Section 4 (Experimental Procedure and Methods).

A laser-selective, ultrafast, convergent manufacturing system, described in our previous papers [22, 26], was used to fabricate alumina specimens to build the training dataset for ML. A high-throughput method was applied, which can fabricate several tens of laser-sintered alumina micro-samples with various hardness at once [22]. The microstructure and microhardness of these micro-samples were then characterized by SEM and microhardness tester, respectively. Each SEM graph (1280×960) was segmented into 256×256 pixels micrographs and enhanced contrast using the adaptive equalization normalization method [27]. Seven groups of various micrographs labeled with different hardness values constructed the ML dataset. All the micrographs in one group are labeled with the same hardness value. Detailed information of the experiments is given in Section 4 (Experimental Procedure and Methods).

In this study, hardness is chosen as the mechanical property for microstructure prediction. For ceramics, hardness is strongly controlled by microstructural features, specifically grain size and porosity [28–30]. In our ML dataset, as shown in Figure 2, the hardness increases as the relative density of laser-sintered alumina increases. In Figure 2, three exemplar SEM micrographs with different microhardness are given: (a) the porous microstructure corresponding to low hardness; (b) the density microstructure corresponding to intermediate hardness; and (c) the close-to-fully dense microstructure corresponding to high hardness.

We chose a small number (seven) of datasets for study to test the model's generalization ability. Six datasets were randomly chosen for training, and one dataset was left for validation. These datasets were sparse and covered a wide range of hardness (i.e., 665–2343 kgf/mm^2). Thus, the micrographs were substantially different. We wanted our GAN models to learn the inherent correlation between hardness and microstructure and predict the significantly different micrographs from the training sets.

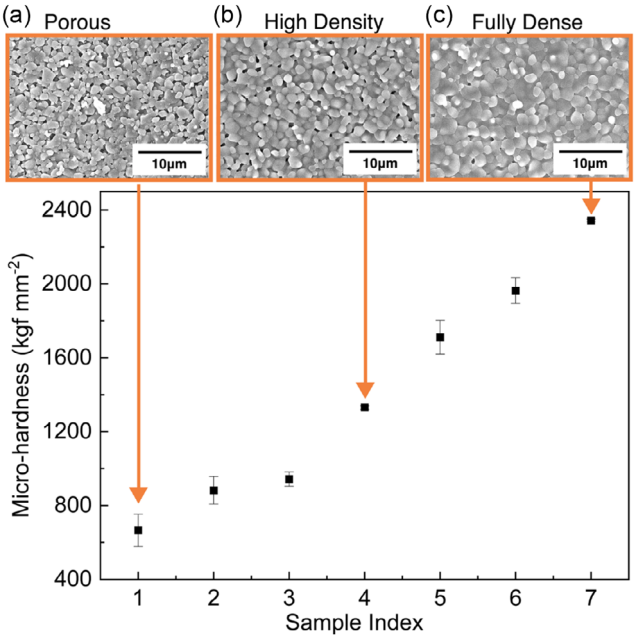

FIGURE 2 | Examples of experimental data that show the strong relationship between microstructure and microhardness of laser-sintered Al_2O_3. For illustration, three microstructures were picked at different hardness: (a) high porosity (hardness 665 kgf mm^{-2}; (b) medium density (hardness 1311 kgf mm^{-2}); and (c) close to fully dense (hardness 2343 kgf mm^{-2}).

We also used a relatively small training data size. Each dataset contained ≈1800 segmented micrographs (256×256 pixels) generated from eight experimentally obtained SEM images (1280×896 pixels) for each hardness. It is essential in this article to demonstrate the optimal architecture of GAN models that can achieve excellent performance with a relatively small number of training data. It is also important to demonstrate that GAN can be trained using experimentally obtained microstructure micrographs with a reasonable workload. For example, collecting eight SEM micrographs per sample can be achieved within a relatively short time.

After training, GAN-based models can synthesize SEM micrographs for target hardness. The generated microstructure image can show various real microstructure features, like grain size, grain distribution, tortuosity, porosity, and so on. To avoid confusion in the rest of this article, the ML-synthesized micrographs under the trained conditions are called "regenerated" micrographs. The ML-generated micrographs under new or unexplored hardness, not in the training dataset, are called "predicted" micrographs.

2.2 | Comparison of the Performance of RCWGAN-GP, RCWGAN-GP-W, and M-GAN in Regeneration and Prediction of SEM Micrographs from Hardness

We found that M-GAN had the best performance among the three algorithms, while RCWGAN-GP had the worst performance. Initially, we built the ML algorithm based on the RCWGAN-GP algorithm, which showed powerful capabilities in predicting 128×128 pixels (the real sample area was 6.4×6.4 μm^2) micrographs for input laser powers during laser-sintering experiments in our previous paper [23]. However, this micrograph size was sometimes too small to obtain statistically meaningful features of microstructure (e.g., grain size). As a result, there was a need to generate larger micrographs. When we trained the RCWGAN-GP algorithm using the 256×256-pixel micrographs, the generated micrographs only roughly captured the porosity and grain size of real SEM for both low and high relative densities (Figure 3a-I and b-I). These regenerated images were noisy no matter how many training episodes were used. Only micrometer-scale features were clear in these images. This poor performance was caused by larger micrographs (256×256 pixels) compared to small micrographs (128×128 pixels) used in our previous paper [23]. The large SEM images contain many microstructural details and features. For example, in the real SEM of porous microstructure (Figure 3a-IV), the spatial distribution of grains is more intricate. Many grains are stacked on top of each other. Grains and pores vary in different ways. These features posed significant challenges for the ML algorithm to learn. As for dense microstructure (Figure 3b-IV), the major features were grain size and grain boundary, while pores were insignificant. Compared to the contrast between grain and pores in porous microstructure images, the contrast between grain and grain boundary was very small in the dense microstructure images. As hardness changed, the microstructure characteristics substantially varied. This large variation also posed challenges for ML algorithms to learn.

A common approach to capture detailed features in the images for a GAN-based algorithm is by increasing the network width or depth [31, 32]. We doubled the width of the network in the generator and discriminator of RCWGAN-GP and obtained RCWGAN-GP-W. Compared to RCWGAN-GP,

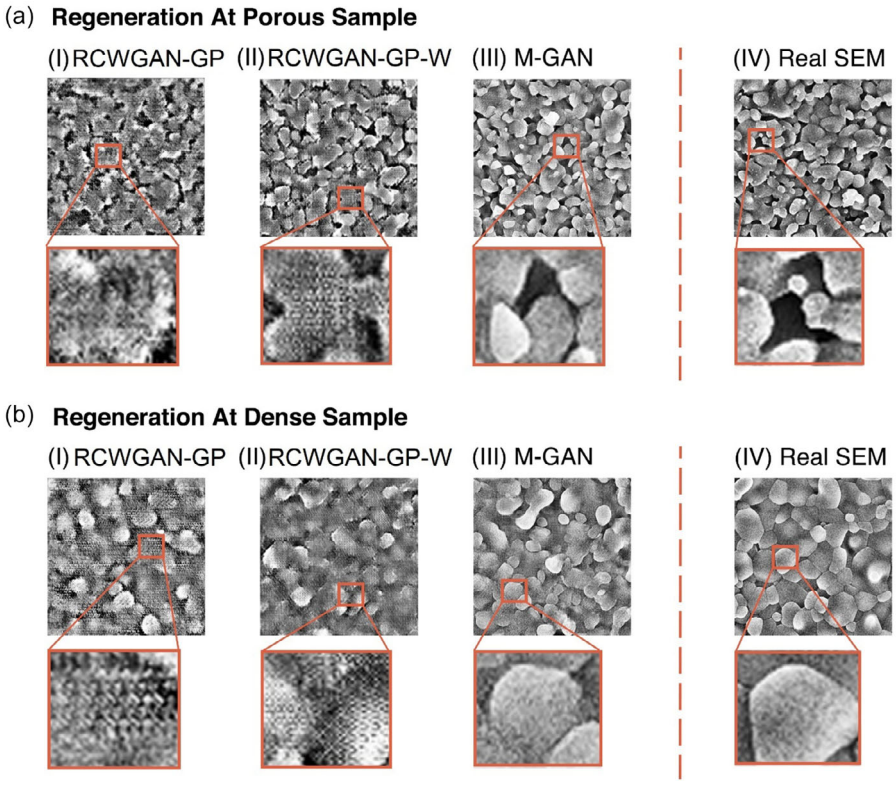

FIGURE 3 | Regenerated micrographs from RCWGAN-GP, RCWGAN-GP-W, and M-GAN with (a) low relative density (at 665 kgf mm^{-2}) and (b) high relative density (at 2343 kgf mm^{-2}). (I) RCWGAN-GP generated low-resolution micrographs with random noises in grain areas. (II) RCWGAN-GP-W generated better-quality images. However, random noises and unclear boundaries still existed. (III) M-GAN generated micrographs with clear grain, grain boundary, and pores. The random noises were insignificant. (IV) As a reference, real SEM micrographs are presented on the right. The zoom-in images of grain areas were marked using orange boxes.

RCWGAN-GP-W-synthesized SEM micrographs have more detailed features of grains and pores. For instance, in Figure 3a-II and b-II, the porosity and grain size were very similar to the ones in the real SEM micrographs. The grain boundary was much clearer and smoother in the regenerated images of the porous sample (Figure 3a-II). Although less obvious, random noises still existed for all image generations using RCWGAN-GP-W, especially for high relative density samples. The grain boundary was blurry and indistinguishable in the regenerated micrographs of highly dense samples (Figure 3b-II). One challenge for RCWGAN-GP-W is that it requires much more computing resources than RCWGAN-GP in training and generation. In RCWGAN-GP, both the discriminator and the generator had about 3 million parameters. However, in RCWGAN-GP-W, the discriminator had more than 12 million parameters, and the generator had about 7 million parameters. The RCWGAN-GP-W doubles the time spent in training and image generation while providing mediocre improvements in image quality.

Recently, residual blocks have been used in GAN-based algorithms to improve the quality of generated images [25, 33]. The residual block structure was inspired by the famous ResNet [34]. In ResNet, it has been shown that training can converge much faster compared to similar structures without residual blocks. Thus, M-GAN training is also expected to converge with relatively small training data size and epoch number. The residual block leverages the technique of identity mapping (also known as skip connection), where the input of the block is added directly to the output, forming two streams of data, one passing two convolutional layers and being processed and one unchanged. During backpropagation, the gradient can skip some blocks and significantly affect the shallower layers. This allows the residual block-based network to combine the advantages of both the deeper network's capturing capability and the shallower network's training stability. As a result, the generated image from the residual blocks modified algorithms can successfully capture the details of the original images and achieve high image quality [25, 32]. Therefore, we developed M-GAN with residual blocks to improve the image generation quality. As shown in Figure 3a-III and b-III, all M-GAN synthesized images showed high image fidelity. Grain boundaries were clear and smooth compared to the results generated using RCWGAN-GP and RCWGAN-GP-W. The distinguishable microstructure features were as clear as the ones in the real SEM images. It indicated that M-GAN synthesized micrographs obtained a quality close to the real SEM micrographs. As for the microstructure features, nano features (≈50 nm) can be distinguished in the M-GAN-generated images. They showed grain size and porosity similar to the real SEM images. Blurry noises in the area of the grains, which were often found in CWGAN-GP-synthesized images, were eliminated.

Since a deeper structure was adopted in M-GAN, its training efficiency was similar to that of the RCWGAN-GP-W and lower than that of RCWGAN-GP. The discriminator had about 14 million parameters, and the generator had about 3 million. However, the image generation time was significantly lower than that of RCWGAN-GP-W because of a smaller generator with fewer parameters. The reduction in the generator's size and significant improvement in image quality shows the efficacy of M-GAN.

2.3 | Regeneration and Prediction of SEM Micrographs Using M-GAN

After training, M-GAN not only regenerated microstructure images corresponding to certain training labels (i.e., hardness values) but also predicted the microstructure for an arbitrary hardness input, which is not in the training set. The results are shown in Figure 4. M-GAN regenerated microstructure images were highly realistic for both low hardness (e.g., 665 kgf mm^{-2}) and high hardness (e.g., 2343 kgf mm^{-2}). Furthermore, the micrographs predicted by M-GAN from the input of 1711 kgf mm^{-2} hardness were also very similar to the actual SEM images in terms of grain size, shape, and porosity. The results show that the M-GAN can learn the trend of relative density and grain size increasing as hardness increases. To achieve such capability in predicting microstructures with an arbitrarily unknown hardness, we only trained M-GAN with six hardness-labeled micrographs data groups, i.e., 665, 882, 943, 1311, 1963, and 2343 kgf mm^{-2}. After training, the M-GAN can predict the SEM micrographs at 1711 kgf mm^{-2}, which is similar to the real SEM of the sample with this hardness (Figure 4).

Another advantage of using M-GAN to predict microstructure is that it can capture the stochastic features of microstructure. Usually, the microstructure varies from position to position within the material. One example of stochastic predictions from M-GAN is given in Figure 5, side by side with experimentally obtained SEM micrographs at various locations for comparison. We found that the actual microstructure had slight spatial variations in the laser-sintering experiments. The second column in Figure 5 shows a tiny difference in porosity and grain size distribution among these three locations. Remarkably, our M-GAN-predicted microstructural images capture this variation in corresponding real SEM micrographs. M-GAN captured important stochastic features of the real microstructure, like grain size, porosity distributions, and other microstructure features.

2.4 | Establishing a Pretrained CNN to Evaluate the Performance of M-GAN

Although M-GAN generates very realistic microstructure images, we still need to develop metrics to evaluate the precision of

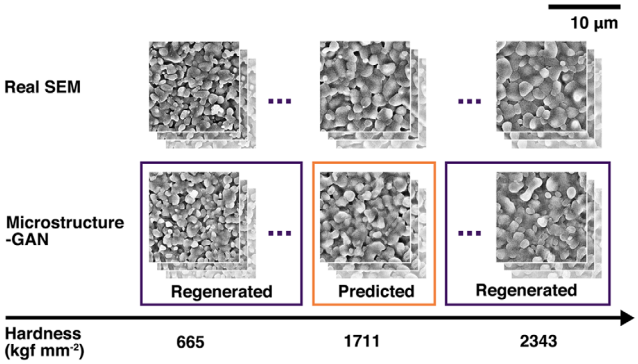

FIGURE 4 | Regenerated and predicted micrographs from M-GAN using different hardness as the inputs. The experimental SEM micrographs are given in the top row for comparison.

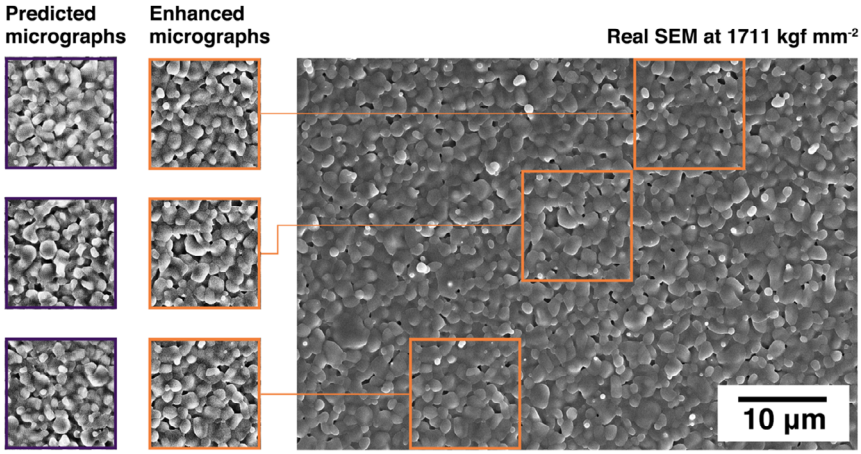

FIGURE 5 | M-GAN predicted micrographs with high similarity to experimental SEM images. Three locations, marked as orange, were picked from one SEM image of the sample with a hardness of 1711 kgf mm^{-2}. Similar predicted images are presented in the first column on the left. Predicted images successfully captured the subtle variation of microstructure captured in the real SEM image.

M-GAN predictions. A pretrained CNN was established to evaluate the hardness for microstructure images and characterize the accuracy of the M-GAN prediction for the target hardness. The scope of this article is to demonstrate the effectiveness of M-GAN in predicting detailed microstructure features based on the hardness input. The microstructure features include both small-scale (nanometer) features and global features (micrometer and above). These features jointly affect the hardness. Thus, we used a pretrained CNN to evaluate the difference between predicted micrographs and experimentally obtained micrographs. The pretrained CNN can capture both localized features and global features. The approach for evaluation is illustrated in Figure 6. This evaluation method is very similar to the "inception score (IS)" method, which is commonly used to evaluate the precision of GANs [35]. Directly using other pretrained models like Inception V3 does not work because they are trained on daily images and are not capable of extracting microstructure features. After training, M-GAN regenerated SEM micrographs for six trained hardness and predicted one group for the target hardness. Each group under one given hardness had 60 generated micrographs. The pretrained CNN evaluated both M-GAN-synthesized SEM micrographs and real ones under the same hardness labels to obtain the corresponding hardness value, H_m and H_{real}. Here, H_m Stands for CNN-evaluated hardness from M-GAN-synthesized micrographs and H_{real} stands for CNN-evaluated hardness from real SEM micrographs. Finally, we compared those two hardness and calculated bias between H_m and H_{real} to validate the M-GAN regeneration and prediction. The architecture of this pretrained CNN is detailed in Section 4.3(Architecture of Pretrained CNN and the Training Processing).

We evaluate the precision of the 'pre-trained' CNN. This CNN was trained using the experimentally obtained SEM micrographs and corresponding hardness. The precision was validated by comparing CNN-predicted and real hardness, as shown in Figure 7. The relative root mean square error (RRMSE) was used for each hardness prediction to quantify the accuracy of pretrained CNN evaluation. The RRMSE for each hardness data group was calculated using the following equation:

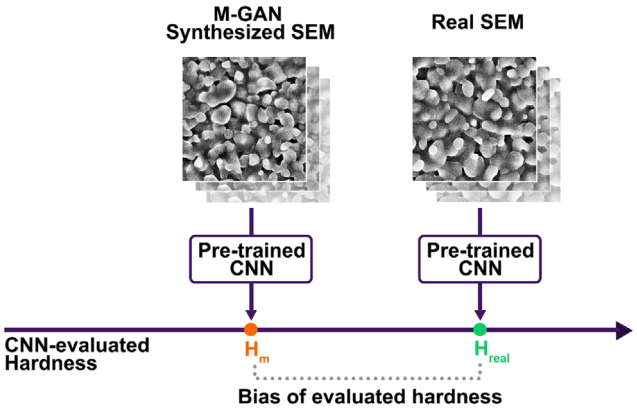

FIGURE 6 | The approach of evaluating the precision of M-GAN in predicting hardness. A pretrained CNN was used to evaluate both M-GAN-synthesized SEM micrographs and real ones. The bias of these two evaluations (H_m, CNN-evaluated hardness from M-GAN synthesized SEM; H_{real}, CNN-evaluated hardness from real SEM) will be used as a metric for validating the M-GAN predictions This CNN was trained from the ML dataset with all the hardness.

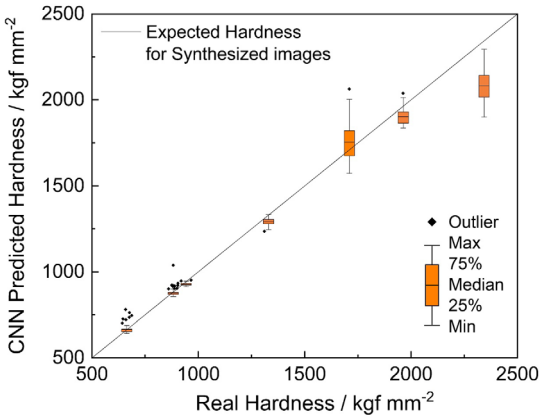

FIGURE 7 | Boxplots of performance validation of pretrained CNN. The X axis is the real hardness for each dataset. The *Y* axis is the CNN-evaluated hardness for the validation dataset. The solid line represents the expected relationship between CNN-evaluated and actual hardness.

TABLE 1 | RRMSE of predicted hardness for each data group.

Hardness (kgf mm^{-2})	665	882	943	1311	1711	1963	2343
RRMSE	1.6%	1.4%	1.8%	3.1%	6.1%	3.9%	11.7%

$$\mathrm{RRMSE} = \frac{\sqrt{\frac{1}{n} \times \sum_{i=1}^{n} \left(H^{i}_{\mathrm{predict}} - H_{\mathrm{experimental}}\right)^{2}}}{H_{\mathrm{experimental}}} \quad (1)$$

where n stands for the total amount of predictions for one specific hardness; H_{predict} is the predicted hardness via pretrained CNN; $H_{\mathrm{experimental}}$ is the experimentally measured hardness for one group dataset.

As shown in Table 1, most of the predicted hardness matched well with the real hardness. The relative RRMSE was within 6.1%, up to 1711 kgf mm^{-2}. Larger deviation of CNN evaluation was observed in high hardness samples (>1711 kgf mm^{-2}). For the highest hardness (i.e., 2343 kgf mm^{-2}), CNN-predicted hardness was much smaller than the real hardness, and the RRMSE was 11.7%. This larger deviation may be caused by a drastic increase in hardness with small changes in the microstructure. As we can see in Figure 8, the microstructure substantially changes as hardness increases from 665 to 1311 kg mm^{-2}, but slightly changes when hardness increases from 1711 to 2343 kg mm^{-2}. This shows that CNN had difficulty in accurately predicting hardness when the SEM micrographs look similar.

2.5 | M-GAN Performance Evaluated Using the Pretrained CNN

The difference between M-GAN-generated micrographs and real ones at the same hardness was evaluated using the pretrained CNN. The plot of H_{m} versus H_{real} is given in Figure 9. Here, H_{m} stands for CNN-evaluated hardness from M-GAN synthesized SEM for one data group. H_{real} stands for average CNN-evaluated hardness from real ones in the same data group.

The data points can be divided into two groups: (1) regenerated SEM micrographs and (2) predicted ones. Two different target hardnesses were evaluated to test the robustness of the M-GAN prediction: 1711 and 943 kgf mm^{-2}. As shown in Figure 9a,b, all CNN-evaluated hardness from M-GAN synthesized micrographs (H_{m}) had values close to the values from real

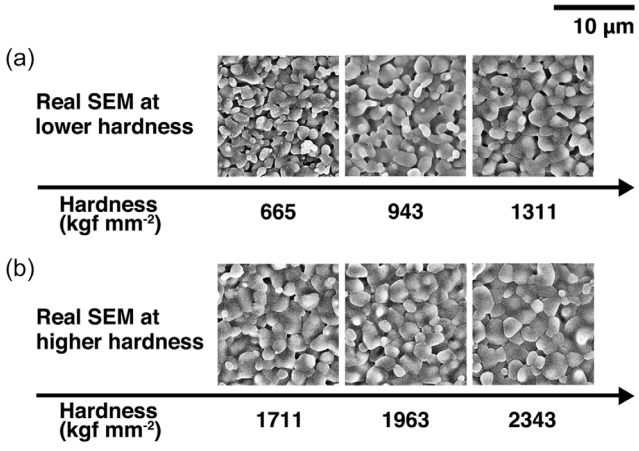

FIGURE 8 | Examples of experimental SEM for (a) lower hardness samples and (b) higher hardness samples. As the alumina samples were sintered to close to fully dense, the hardness increased significantly without significant change in microstructure.

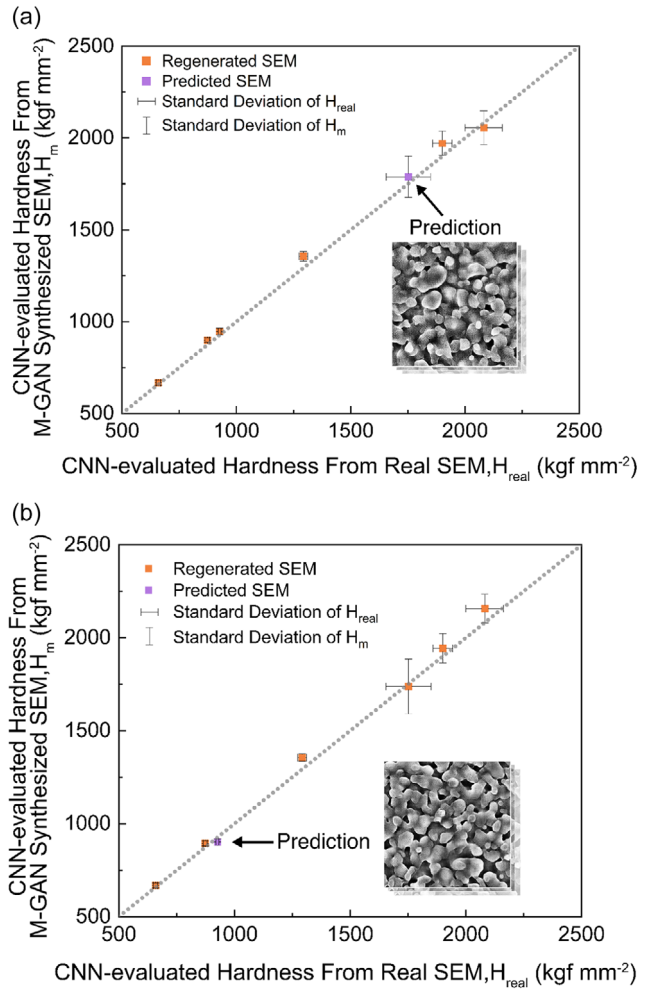

FIGURE 9 | The pretrained-CNN-evaluated hardness from real SEM (H_{real}) and M-GAN synthesized SEM (H_{m}). Different prediction targets were picked to test the robustness of M-GAN predictions: (a) at 1711 kgf mm^{-2}; (b) at 943 kgf mm^{-2}. M-GAN synthesized 60 μg at seven different hardness. Next, the pretrained CNN evaluated the hardness of each micrograph. The evaluated hardness of regenerated micrographs is plotted in orange, while the predicted micrographs are plotted in purple. Predicted SEM are also displayed for reference. The dashed line shows equal values of H_{real} and H_{m}. The standard deviation of each hardness is also shown in the figure.

SEM (H_{real}). The dashed line indicated the equal values for H_m and H_{real}. For all regenerated micrographs, their H_m obtained similar values to the corresponding H_{real}, including the ones at 2343 kgf mm^{-2}.

The relative bias was used to show the difference between M-GAN synthesized SEM and real SEM. It was defined as the following equation:

$$\text{Relative Bias} = \left| \frac{\overline{H}_m - \overline{H}_{real}}{\overline{H}_{real}} \right| \quad (2)$$

Here, $\overline{H}_m$ is the average H_m and $\overline{H}_{real}$ is the average H_{real}.

The statistical data of the CNN evaluations and relative biases are summarized in Table 2. The relative biases were all within 4.9% for both cases. The M-GAN-regenerated SEM micrographs matched well with the corresponding real ones. Although the CNN showed large errors for evaluating high-hardness micrographs (e.g., 2343 kgf mm^{-2}, as shown in Figure 7), the CNN evaluation for M-GAN-regenerated micrographs was close to the evaluation for real images in the hardness range from 1711 to 2342 kgf mm^{-2}. This indicates that the pretrained CNN can barely distinguish the M-GAN-generated micrographs and real ones at the high hardness range.

For the M-GAN-predicted micrographs, the CNN evaluations were very close to the evaluation of real images. The relative bias for the prediction at 1711 and at 943 kgf mm^{-2} was 2.1% and 2.7%, respectively. This result indicated a high accuracy of prediction from M-GAN. M-GAN showed good performance in prediction both porous and dense microstructures.

3 | Conclusion

This study demonstrated a high-performance microstructure image prediction model, M-GAN. Using target hardness as an input, our ML algorithm can predict highly realistic microstructure images. This M-GAN was built upon our previous algorithm (RCWGAN-GP). M-GAN showed significant improvement from RCWGAN-GP in microstructure prediction for large-area microstructure micrographs (256 × 256 pixels). The M-GAN can synthesize high-fidelity, detailed, feature-rich microstructure images indistinguishable from the experimentally obtained SEM micrographs. The recognizable microstructural features are at different length scales, including nanometer scale (≈50 nm) in 12.8 × 12.8 μm micrographs. The synthesized images successfully captured several important features of laser-sintered alumina microstructure, like grain size, porosity, grain surface features, and even local microstructural variation.

A pretrained CNN network was built to validate M-GAN prediction and regeneration. The CNN can barely distinguish between predicted/regenerated images and real ones. We tested two prediction scenarios: 1711 and 943 kgf mm^{-2}. The relative biases of all regenerated and predicted images were within 4.9%. These results validate the accuracy of M-GAN for both regeneration and prediction of microstructural images for a given hardness.

In conclusion, M-GAN regenerated and predicted highly realistic SEM micrographs for various hardnesses. This provides an important tool for predicting microstructure for specific microstructure-sensitive properties, like hardness.

TABLE 2 | CNN-evaluated hardness for each data group with twodifferent prediction targets: (a) 1711 kgf mm^{-2} and (b) 943 kgf mm^{-2}.

	CNN evaluation for real images (kgf mm^{-2})	CNN evaluation for M-GAN-generated images (kgf mm^{-2})	Relative bias
(a) Prediction target: 1711 kgf mm^{-2}			
Regeneration	659 ± 10	668 ± 13	1.4%
	874 ± 9	900 ± 11	3.0%
	927 ± 6	946 ± 18	2.0%
	1293 ± 19	1356 ± 26	4.9%
Prediction	1752 ± 97	1789 ± 112	2.1%
Regeneration	1900 ± 42	1971 ± 66	3.7%
	2082 ± 81	2055 ± 93	1.3%
(b) Prediction target: 943 kgf mm^{-2}			
Regeneration	659 ± 10	668 ± 12	1.3%
	874 ± 9	894 ± 13	2.3%
Prediction	927 ± 6	901 ± 16	2.7%
Regeneration	1293 ± 19	1356 ± 20	4.6%
	1752 ± 97	1738 ± 148	0.8%
	1900 ± 42	1943 ± 78	2.2%
	2082 ± 81	2157 ± 77	3.6%

4 | Experimental Procedure and Methods

4.1 | ML Dataset Construction Using the Laser-Based High-Throughput Method

To collect the data for the ML training, we prepared a sample array containing approximately 80 sample units using the laser-based high-throughput method [22], as shown in Figure 10. Then, we characterized the microstructure and microhardness of these sample units. The micro-sample unis with various microstructures were laser sintered in one scan. The SEM micrographs and microhardnesses were characterized for each sample unit. This study selected the material feature data (i.e., SEM micrographs and hardnesses) of 7 micro-samples due to their apparent differences.

4.1.1 | Laser-Based High-Throughput Micro-Sample Fabrication

Here, we summarize the experimental procedure. Full details are in Ref. [22]. Alumina paste was prepared by mixing 79.75 wt.% Al_2O_3 powder (Almatis A152SG, $d_{50} = 1.2$ μm, purity: 99.8%) with 0.1 wt% dispersant (Darvan 821A), 20.0 wt% deionized water, and 0.15 wt% binder (hydroxypropyl) methyl cellulose, and ball-milled for 48 h. And, ≈500 μm thickness alumina paste film was deposited on a silica substrate. The green (unsintered) alumina film was dried in a controlled environment and then micromachined using a picosecond laser (PXxxx-1, wavelength 1048μm, EdgeWave, Inc., San Diego, CA, USA) into square arrays with each unit of 450 × 450 μm.

This micromachined green alumina sample array was sintered using a CO_2 laser (Firestar v20, wavelength 10.6 μm, SYNRAD, Inc., Mukilteo, WA, USA), with a cylindrical lens (focal length 25.4 mm, diameter 19.05 mm, Laser Mechanisms, Inc., Novi, MA, USA). The cylindrical lens resulted in a line-shaped laser beam, such that the width of the laser beam (≈8 mm long) covered the entire area of the sample array when the laser scanned along the sample length of the array. The laser power was 64.5 W, and the laser scanning rate was 0.1 mm/s. Due to the Gaussian distribution of the laser power, this single scan generated sintered samples with a broad range of density, microstructure, and hardness.

4.1.2 | Microstructure and Hardness Characterization

The microstructure was characterized using the SEM (Hitachi S4800, Hitachi, Ltd., Tokyo, Japan, and Hitachi S6600, Hitachi, Ltd., Tokyo, Japan). The microhardness of laser-sintered alumina arrays was characterized using a microhardness tester (MHT-210 microhardness tester, LECO Corporation, St. Joseph, MI, USA). Vickers indentation was introduced on the sample surface, and its size was measured on SEM-generated micrographs. The magnification of each SEM image is kept at 2000×. Each image had 1280 × 896 pixels. In total, 59 SEM images with 7 different hardness were collected for the ML dataset. A total of 59 different SEM images were labeled with their corresponding hardness.

4.1.3 | Data Process for ML Training

To augment data for ML training, the SEM images were cropped into smaller sub-micrographs of 256 × 256 pixels (corresponding to a real area of 12.8 × 12.8 μm^2). To further augment the dataset, we rotate every image by 90°, 180°, and 270°. As a result, the number of images quadrupled. As a result, 12,744 segmented images were obtained.

All the images were contrast-enhanced using adaptive equalization normalization [36]. This normalization eliminated the brightness difference among different SEM images, resulting in enhanced micro-images with similar brightness. In addition, the contrast of each image was also enhanced, which is beneficial for algorithm training.

4.2 | Architecture of RCWGAN-GP, RCWGAN-GP-W, M-GAN, and the Training Processing

4.2.1 | RCWGAN-GP

Our previous papers demonstrated that RCWGAN-GP satisfactorily predicts the material's microstructure for arbitrary processing conditions [18, 23]. The CGAN consists of a discriminator and a generator and trains them to play a minimax game described by the following objective function:

$$\min_G \max_D \left\{ E_{\boldsymbol{x}|y\sim P_r}[D(\boldsymbol{x},y)] - E_{z\sim p_z}[D(G(\boldsymbol{z},y),y)] \right\} \quad (3)$$

where $\boldsymbol{x}$ represents a microstructure image, y is the processing parameter or condition, $\boldsymbol{x}|y \sim P_r$ means the conditional distribution of $\boldsymbol{x}|y$ is P_r, resembled by the collected experimental data, $\boldsymbol{z}$ is a random seed drawn from a multivariant Gaussian distribution, $D(\boldsymbol{x},y)$ is the validity score produced by the discriminator using $\boldsymbol{x}$

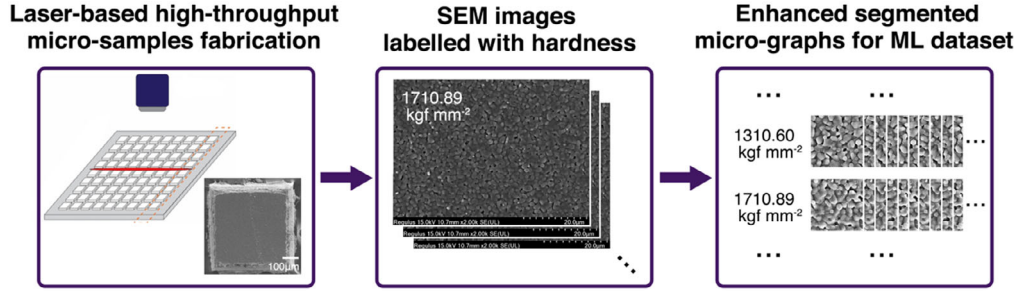

FIGURE 10 | ML database construction. Alumina micro-samples were fabricated using a laser-based high-throughput method. Then, each sample was characterized using SEM and a microhardness tester.

and y as inputs, and $G(\boldsymbol{z},y)$ is a generated microstructure image produced by the generator from the random seed and the condition.

Once the CGAN is well trained, the generated microstructural images $\hat{x}|y$ follows a distribution P_g that is close to the real distribution P_r. Suppose a microstructure feature (e.g. porosity) can be quantified from a microstructure image using a predefined measurement $f(\cdot)$.

$$MF = f(\boldsymbol{x}) \tag{4}$$

MF is the microstructure feature.

The relationship between the microstructure feature and the processing parameter y can be written as

$$MF(y) = E_{\boldsymbol{x}|y\sim P_r}[f(\boldsymbol{x}|y)] \tag{5}$$

Since the real microstructure distribution P_r can be well approximated using P_g, the relationship between the microstructure feature and the processing parameter can also be approximated as

$$MF(y) \approx E_{\hat{x}|y\sim P_g}[f(\hat{x}|y)] = E_{(z\sim p_z)}(f(G(\boldsymbol{z},y))) \tag{6}$$

Or empirically

$$MF(y) = \frac{1}{N}\sum_{i}^{N} f(G(\boldsymbol{z}_i,y)) \tag{7}$$

This means that for an arbitrary processing parameter y, the microstructure feature can be calculated by sampling N random seeds, using the generator to produce N microstructural images, and measuring them. Thus, we can call CGAN regression-based CGAN (RCGAN) if we predict the microstructure from an arbitrary condition.

We can improve the performance of RCGAN with the Wasserstein loss function [37]. The improved algorithm is known as regression-based, conditional Wasserstein GAN (RCWGAN). Significant improvement was found for RCWGAN in microstructure predictions as shown in our previous study [18]. The microstructural features of grains and pores can be observed in the synthesized SEM micrographs. However, the grain boundaries and 3D configuration of the grains were still unclear. The regenerated microstructures had larger apparent average particle size than the real SEM. These defects might originate from the weight-clipping technique used in the RCWGAN [25]. Finally, we replaced weight clipping with gradient penalty [38] and developed an RCWGAN-GP algorithm for our simulation and prediction.

4.2.2 | Architecture of RCWGAN-GP and RCWGAN-GP-W

The architecture of the generator and discriminator in our RCWGAN-GP algorithm is shown in Figure 11. The generator had two inputs (Figure 11a). One was a random vector used as a seed for image generation. The other was the conditioning input, a single scalar value (e.g., normalized hardness value). In the generator, the seed was expanded by a dense layer and then reshaped into $8\times8\times128$. The condition was also expanded by a dense layer and then reshaped into $8\times8\times16$. Then they were concatenated together and reshaped to $256\times256\times8$ through six convolutional layers (Conv). Finally, using another special conventional layer with tanh as an activation function (Conv, tanh), the input data was reshaped into $256\times256\times1$. As a result, the output was a 256×256 pixels image. All the activation functions used in normal convolution layers were LeakyReLUs defined as

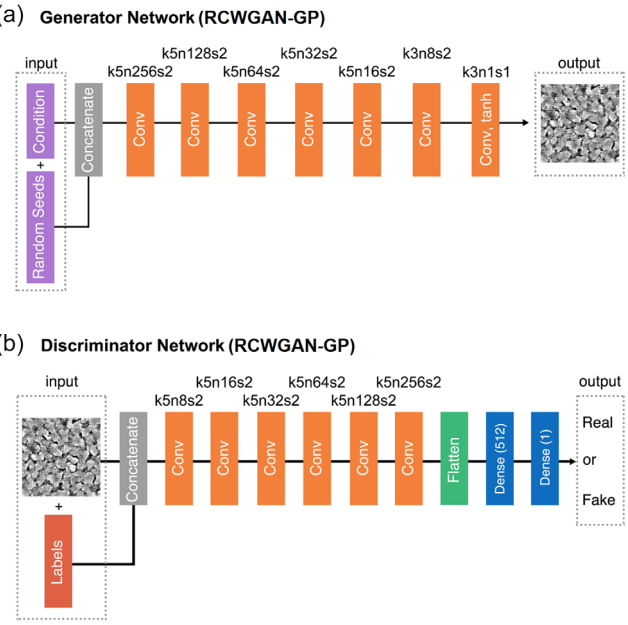

FIGURE 11 | The architecture of (a) generator and (b) discriminator network in RCWGAN-GP with corresponding kernel size (k), number of feature maps (n), and stride (s) indicated for each convolutional layer.

$$f(x) = \max(\alpha x, x) \tag{8}$$

where α was set to be 0.2. The architecture details are shown in Figure 12a.

The discriminator also had two inputs. One is the 256×256 pixels image, and the other is the hardness label. Two inputs concatenated together and reshaped to $4\times4\times256$ via six convolutional layers. Then, input data was flattened by a flatten layer and expanded by two dense layers. The final output is a scaler. The details of the architecture are shown in Figure 11b. The kernel size, numbers of feature maps, and strides used in the convolutional layer were marked as k, n, and s, respectively. In total, the generator and discriminator in CWGAN-GP owned 2 842 785 parameters and 3 323 369 parameters, respectively.

For RCWGAN-GP-W (wide), the major structure was kept the same as the one in RCWGAN-GP, but the number of feature maps (n) in convolutional layers (conv) was doubled in both the generator and discriminator. As a result, the generator had 7 034 433 parameters, and the discriminator had 12 892 369 parameters.

4.2.3 | Architecture of M-GAN

The architecture of the generator and discriminator in the or M-GAN algorithm developed in this study is shown in

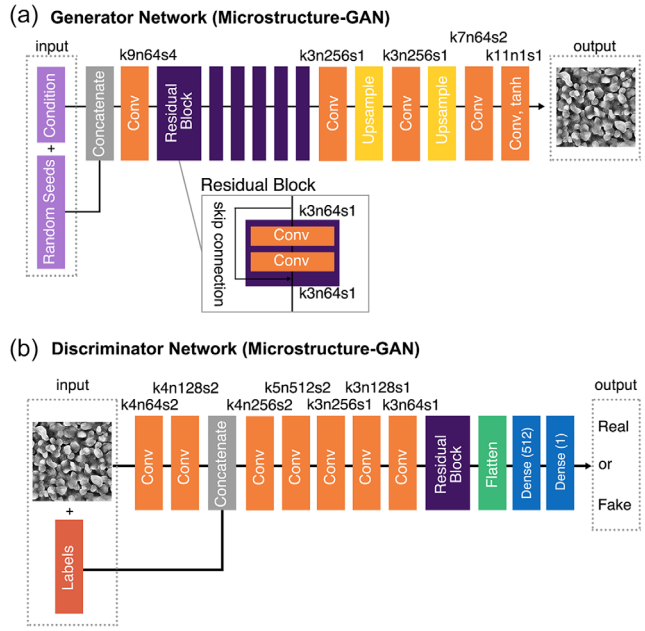

FIGURE 12 | The architecture of (a) generator and (b) discriminator network in Microstructure-GAN (M-GAN) with corresponding kernel size (k), number of feature maps (n), and stride (s) indicated for each convolutional layer.

(Figure 12). Similar to RCWGAN-GP-W, in the generator, one random vector (seed) and one single scalar (condition) were used as input. In the generator, six residual blocks followed the convolutional layer. One residual block was made of two same convolutional layers. Its input was skip-connected to the output. After six residual blocks, the feature map's shape was still kept as $32 \times 32 \times 64$. Using residual blocks, the depth of the network can be greatly increased. As a result, it improves the training efficiency and generation quality. Then, input data was reshaped into $256 \times 256 \times 64$, via three convolutional layers and two upsampling layers. The details of the architecture are shown in Figure 12a.

Like RCWGAN-GP-W, the discriminator also had two inputs. One was the 256×256 pixels image, and the other was the hardness label. The image was reshaped by two convolutional layers into $64 \times 64 \times 128$. The hardness label was expanded by a dense layer and reshaped into $64 \times 64 \times 20$ via one convolutional layer. Then, two inputs were concatenated together and reshaped to $16 \times 16 \times 64$ via five convolutional layers and one residual block. This residual block had the same structure as mentioned earlier. Next, the input data was flattened by a flatten layer and expanded by two dense layers. The final output is a scaler. The details of the architecture are shown in Figure 12b.

4.2.4 | The Training Process

The same training process was applied in RCWGAN-GP, RCWGAN-GP-W, and M-GAN. When training the generator, the loss function was defined as

$$L_g = -E_{\tilde{x}|y\sim P_g}[D(\tilde{x},y)] \tag{9}$$

where $\tilde{x}$ is a generated image, y is the condition, and P_g represents the generator distribution. $D(\tilde{x},y)$ is the output of the discriminator. When training the discriminator, we used the loss function, which was mentioned in our previous works [18, 23]:

$$\begin{aligned} L_d = {} & E_{\tilde{x}|y\sim P_g}[D(\tilde{x},y)] - E_{x|y\sim P_r}[D(\tilde{x},y)] \\ & + \lambda E_{\hat{x}|y\sim P_{\hat{x}}}[(\|\nabla_{\hat{x}} D(\hat{x},y)\|_2 - 1)^2] \end{aligned} \tag{10}$$

where x is a real image, $\tilde{x}$ is a generated image, y is the condition, and P_g and P_r represent the generator distribution and the real data distribution, respectively. The third term is the gradient penalty term. $P_{\hat{x}}$ is uniformly sampling along the straight line between x and $\tilde{x}$. Thus, $\hat{x}$ is calculated as the following:

$$\hat{x} = \epsilon x + (1-\epsilon)\tilde{x} \tag{11}$$

where ϵ is a random number that is uniformly distributed on [0,1]. λ is a hyperparameter that controls the weight of the gradient penalty loss. In this article, it is set to be 1.

We used the Adam optimizer while training the generator and the discriminator. The learning rate is $1E-4$ for the generator and $2E-5$ for the discriminator. We used the mini-batch gradient descent method, where the size of one mini-batch is 128. We trained the algorithm for 800 epochs on Palmetto, the high-performance computing cluster of Clemson University. The M-GAN results reported in this article took 68 h on 40 CPUs and 2 GPUs (Nvidia V100).

4.3 | Architecture of Pretrained CNN and the Training Processing

We use a pretrained CNN to validate the precision of GAN-based models. The architecture of pretrained CNN, used for predicted hardness, is shown in (Figure 13). This CNN's network is similar to our M-GAN's discriminator, with seven convolutional layers, one residual block, one flatten layer, and two dense layers. This CNN only has one input, the 256×256 pixels image. The input image went through seven convolutional layers and one residual block. Then, it was flattened by a flatten layer and expanded by two dense layers. The final output was a scaler, which is predicted hardness of the correlated microstructural image. Adam

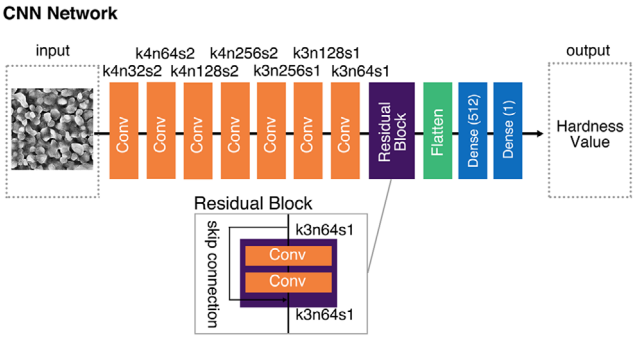

FIGURE 13 | The architecture of CNN with corresponding kernel size (k), number of feature maps (n), and stride (s) indicated for each convolutional layer.

optimizer was used during CNN training. The learning rate is 1E − 4. We used mini-batch gradient descent method, where the size of one mini-batch is 512.

Acknowledgements

The authors acknowledge the funding support from US Army, grant no. W911NF-23-2-0058; US Department of Energy, National Energy Technology Lab, grant no. DE-FE0032231; US Department of Energy, Office of Energy Efficiency & Renewable Energy, grant no. DE-EE0011323; US National Institute of Health, grant no. P20GM121342; and US National Science Foundation, grant no. 2119833.

Conflicts of Interest

The authors declare no conflicts of interest.

Data Availability Statement

The data that support the findings of this study are available from the corresponding author upon reasonable request.

References

1. R. F. Cook, B. R. Lawn, and C. J. Fairbanks, "Microstructure-Strength Properties in Ceramics: I, Effect of Crack Size on Toughness," *Journal of the American Ceramic Society* 68, no. 11 (1985): 604–615.

2. J. M. Fernández, A. Munoz, A. R. de Arellano López, F. V. Feria, A. Dominguez-Rodriguez, and M. Singh, "Microstructure-Mechanical Properties Correlation in Siliconized Silicon Carbide Ceramics," *Acta Materialia* 51, no. 11 (2003): 3259–3275.

3. A. Gupta, A. Cecen, S. Goyal, A. K. Singh, and S. R. Kalidindi, "Structure-Property Linkages Using a Data Science Approach: Application to a Non-Metallic Inclusion/Steel Composite System," *Acta Materialia* 91 (2015): 239–254.

4. N. Hansen, "Hall-Petch Relation and Boundary Strengthening," *Scripta Materialia* 51, no. 8 (2004): 801–806.

5. A. I. Ioffe, M. V. Inozemtsev, A. S. Lipilin, M. V. Perfilev, and S. V. Karpachov, "Effect of the Grain Size on the Conductivity of High-Purity Pore-Free Ceramics Y_2O_8–ZrO_2," *Physica Status Solidi (a)* 30, no. 1 (1975): 87–95.

6. G. M. Christie and F. P. F. Van Berkel, "Microstructure—ionic Conductivity Relationships in Ceria-Gadolinia Electrolytes," *Solid State Ionics* 83, no. 1-2 (1996): 17–27.

7. C. Santoro, A. Agrios, U. Pasaogullari, and B. Li, "Effects of Gas Diffusion Layer (GDL) and Micro Porous Layer (MPL) on Cathode Performance in Microbial Fuel Cells (MFCs," *International Journal of Hydrogen Energy* 36, no. 20 (2011): 13096–13104.

8. F. Zhang, D. Pant, and B. E. Logan, "Long-Term Performance of Activated Carbon Air Cathodes with Different Diffusion Layer Porosities in Microbial Fuel Cells," *Biosensors and Bioelectronics* 30, no. 1 (2011): 49–55.

9. W. Pabst, E. Gregorová, and G. Tichá, "Elasticity of Porous Ceramics—A Critical Study of Modulus–Porosity Relations," *Journal of the European Ceramic Society* 26, no. 7 (2006): 1085–1097.

10. M. Asmani, C. Kermel, A. Leriche, and M. Ourak, "Influence of Porosity on Young's Modulus and Poisson's Ratio in Alumina Ceramics," *Journal of the European Ceramic Society* 21, no. 8 (2001): 1081–1086.

11. K. Guo, Z. Yang, C. H. Yu, and M. J. Buehler, "Artificial Intelligence and Machine Learning in Design of Mechanical Materials," *Materials Horizons* 8, no. 4 (2021): 1153–1172.

12. Z. L. Wang and Y. Adachi, "Property Prediction and Properties-to-Microstructure Inverse Analysis of Steels by a Machine-Learning Approach," *Materials Science and Engineering: A* 744 (2019): 661–670.

13. S. Noguchi and J. Inoue, "Stochastic Characterization and Reconstruction of Material Microstructures for Establishment of Process-Structure-Property Linkage Using the Deep Generative Model," *Physical Review E* 104, no. 2-2 (2021): 025302.

14. S. Chun, S. Roy, Y. T. Nguyen, J. B. Choi, H. S. Udaykumar, and S. S. Baek, "Deep Learning for Synthetic Microstructure Generation in a Materials-by-Design Framework for Heterogeneous Energetic Materials," *Scientific Reports* 10, no. 1 (2020): 13307.

15. R. Narikawa, Y. Fukatsu, Z. L. Wang, et al., "Generative Adversarial Networks-Based Synthetic Microstructures for Data-Driven Materials Design," *Advanced Theory and Simulations* 5, no. 5 (2022): 2100470.

16. Z. Yang, X. Li, L. Catherine Brinson, A. N. Choudhary, W. Chen, and A. Agrawal, "Microstructural Materials Design via Deep Adversarial Learning Methodology," *Journal of Mechanical Design* 140, no. 11 (2018): 111416.

17. I. Goodfellow, J. Pouget-Abadie, M. Mirza, et al., "Generative Adversarial Nets. *Advances in Neural Information Processing Systems*," *Advances in Neural Information Processing Systems* 27 (2014).

18. J. Tang, X. Geng, D. Li, et al., "Machine Learning-Based Microstructure Prediction during Laser Sintering of Alumina," *Scientific Reports* 11, no. 1 (2021): 10724.

19. C. H. Yang, B. S. S. Pokuri, X. Y. Lee, et al., "Multi-Fidelity Machine Learning Models for Structure-Property Mapping of Organic Electronics," *Computational Materials Science* 213 (2022): 111599.

20. X. Y. Lee, J. R. Waite, C. H. Yang, et al., "Fast Inverse Design of Microstructures via Generative Invariance Networks," *Nature Computational Science* 1, no. 3 (2021): 229–238.

21. J. Li, H. Ye, X. Zhang, and N. Wei, "Adjustable Mechanical Properties Design of Microstructure by Using Generative and Adversarial Network with Gradient Penalty," *Mechanics of Advanced Materials and Structures* (2022): 1–12.

22. X. Geng, J. Tang, B. Sheridan, et al., "Ultra-Fast Laser Fabrication of Alumina Micro-Sample Array and High-Throughput Characterization of Microstructure and Hardness," *Crystals* 11, no. 8 (2021): 890, https://doi.org/10.3390/cryst11080890.

23. J. Tang, S. Sarkar, H. Huang, et al., "Online Estimation of Ceramic's Microstructure upon the Laser Spot Brightness during Laser Sintering," *Engineered Science* 22 (2023): 855, https://doi.org/10.30919/es8d855.

24. K. Simonyan and A. Zisserman, "*Very Deep Convolutional Networks for Large-Scale Image Recognition*, arXiv preprint arXiv:1409.1556.

25. C. Ledig, L. Theis, F. Huszár, et al., "*Photo-Realistic Single Image Super-Resolution Using a Generative Adversarial Network*," in Proceedings of the IEEE Conference on Computer Vision and Pattern Recognition (IEEE, 2017), 4681–4690.

26. X. Geng, Y. Hong, J. Lei, et al., "Ultra-Fast, Selective, Non-Melting, Laser Sintering of Alumina with Anisotropic and Size-Suppressed Grains," *Journal of the American Ceramic Society* 104, no. 5 (2021): 1997–2006.

27. S. M. Pizer, et al., "Adaptive Histogram Equalization and Its Variations," *Computer Vision, Graphics, and Image Processing* 39, no. 3 (1987): 355–368.

28. P. M. Sargent and T. F. Page, "Influence of Microstructure on the Microhardness of Ceramic Materials," *Proceedings of the British Ceramic Society*. 26 (1978): 209-224.

29. A. Krell and S. J. M. S. Schädlich, "Nanoindentation Hardness of Submicrometer Alumina Ceramics," *Materials Science and Engineering: A* 307, no. 1-2 (2001): 172–181.

30. Q. Tang and J. Gong, "Effect of Porosity on the Microhardness Testing of Brittle Ceramics: A Case Study on the System of NiO-ZrO2," *Ceramics International* 39, no. 8 (2013): 8751–8759.

31. M. Tan and Q. Le, "*Efficientnet: Rethinking Model Scaling for Convolutional Neural Networks*," in International Conference on Machine Learning, (PMLR, 2019), 6105–6114.

32. T. Nguyen, M. Raghu, and S. Kornblith, "*Do Wide and Deep Networks Learn the Same Things? Uncovering How Neural Network Representations Vary with Width and Depth*," (2020), arXiv preprint arXiv:2010.15327.

33. X. Zhang, C. Feng, A. Wang, L. Yang, and Y. Hao, "CT Super-Resolution Using Multiple Dense Residual Block Based GAN. Signal," *Image and Video Processing* 15 (2021): 725–733.

34. K. He, X. Zhang, S. Ren, and J. Sun, "*Deep Residual Learning for Image Recognition*," in Proceedings of the IEEE Conference on Computer Vision and Pattern Recognition (IEEE, 2016), 770–778.

35. C. Szegedy, V. Vanhoucke, S. Ioffe, J. Shlens, and Z. Wojna, "*Rethinking the Inception Architecture for Computer Vision*," in Proceedings of the IEEE Conference on Computer Vision and Pattern Recognition (IEEE, 2016), 2818–2826.

36. S. M. P., "Adaptive Histogram Equalization and Its Variations," *Computer Graphics and Image Processing* 6 (1977): 184–195.

37. M. Arjovsky, S. Chintala, and L. Bottou, "*Wasserstein Generative Adversarial Networks*," in International Conference on Machine Learning, (PMLR, 2017), 214–223.

38. I. Gulrajani, F. Ahmed, M. Arjovsky, V. Dumoulin, and A. C. Courville, *Improved Training of Wasserstein Gans.*, Advances in Neural Information Processing Systems 30, (2017).